A Digital Prism-based Wavefront Sensor Testbench

Byron Engler[a], Steve Weddell[a], and Richard Clare[a]

[a]Department of Electrical and Computer Engineering, Private Bag 4800, Christchurch, New Zealand

ABSTRACT

In this paper, we present a simulation framework for a digital prism-based wavefront sensor. In simulation, we generate a digital prism wavefront sensor (3-sided, 4-sided and cone) and compute the linearity of the 3-sided digital prism wavefront sensor to the defocus aberration. We then use the same simulation tools, replacing the prism WFS phase map with a spatial light modulator in a laboratory set-up. This allows us to create a digital prism-based wavefront sensor in the laboratory. We then evaluate the linearity of a real 3-sided digital prism-based wavefront sensor and compare with our simulations.

1. INTRODUCTION

The 4-sided (pyramid) prism wavefront sensor (WFS) was first introduced by Ragazzoni[1] in 1996. Since then, variations to the geometry have been proposed (two 2-sided roofs, 3-sided, 6-sided and a cone[2,3]). These variants of the original pyramid have been compared in simulation[3,4] but not in a physical system. In a real adaptive optics system, in order to evaluate different prism geometries (number of side and apex angle), a new prism will need to be manufactured for each new geometry evaluated. This is both expensive and time consuming. In simulation, the prism is represented as a map of optical phase delay. A device called a spatial light modulator (SLM), which is similar to a liquid crystal display, allows a programmable phase delay at each pixel. This allows for a wide range of prism geometries to be generated and the prism geometries can be changed on-the-fly. This was first used by Akondi[5] to create a digital pyramid wavefront sensor.

In this paper, we simulate our digital prism wavefront sensor, with 3-sided, 4-sided and cone geometries, in ideal conditions (not including limitations of the SLM). We then take into account the limitations of the SLM, such as pixel size and maximum phase delay per pixel. The phase delay required to produce a useful prism is much larger than the maximum programmable phase delay on each pixel. To overcome this, the prism phase map must be wrapped. The phase wrapping introduces diffraction artefacts, which if not accounted for, can interfere with the pupil images created by the prism WFS.

Using the same prism phase maps from the simulations, an SLM is used to create the prism WFSs in the optics laboratory. We measure the linear range of the 3-sided prism, for a defocus aberration. The aberration is introduced by a deformable mirror (DM). We then compare the simulated results with the laboratory results.

The different geometry prisms are interesting, as reducing the number of sides improves manufacturability and for the 3-sided prism, the light is spread over less area, resulting in a higher signal-to-noise(SNR) ratio. Increasing the number of prism sides, more information about the incoming wavefront could be measured but at a reduced SNR. Using a digital prism WFS, we can quickly evaluate these trade-offs in a real system.

In Section 2, we show how the prism-based WFS is represented in simulation. The results of simulating the 3-sided prism, 4-sided prism and cone WFS are shown in Section 3 as well as how the effects of the SLM were accounted for in the simulation. The experimental results of the digital prism-based WFS are shown in Section 4.

Further author information: (Send correspondence to Byron Engler)
E-mail: byron.engler@pg.canterbury.ac.nz

2. METHODOLOGY

The prism placed at the focal plane of a telescope can be described as a phase delay map, $H(u,v)$. The light propagates through the prism phase map and through relay optics and onto the detector. The image plane formed at the detector $I(x,y)$ is defined by,[2]

$$I(x,y) = \left| \mathcal{F}^{-1}\Big[H(u,v) \times \mathcal{F}\Big[P(x,y)\exp[j\phi(x,y)] \Big] \Big] \right|^2, \tag{1}$$

where $\phi(x,y)$ is the phase of the incoming wavefront and $P(x,y)$ defines the telescope pupil. The phase delay map for an N-sided prism is described by,[6]

$$H_N(u,v) = \exp\left[jb \frac{\max\{\hat{k}_1 \cdot \vec{g}, \cdots, \hat{k}_N \cdot \vec{g}\}}{\sin(\frac{\pi}{N})} \right], \tag{2}$$

where $\hat{k_N}$ is a unit vector pointing in the direction of a N^{th} side of the prism, $\vec{g}$ is a vector from the origin of the phase map to a point, $F(u,v)$, in the phase map and b is the slope of the prism face. A graphical representation of the formation of the $\hat{k_N}$ and $\vec{g}$ vectors is shown in Fig. 1 This works for the three and four sided prisms. The cone phase delay map is defined as,[2]

$$H_\infty(u,v) = \exp[j2\pi b\sqrt{(|u^2| + |v^2|)}]. \tag{3}$$

Using Eqs. 3 and 2, the phase delay maps for a 3-sided prism, 4-sided prism and cone are generated. The resulting phase maps are shown in Fig. 2. Using the prism phase maps, the resulting detector image can be calculated using Eq. 1. The resulting detector plane images are shown in Fig. 3.

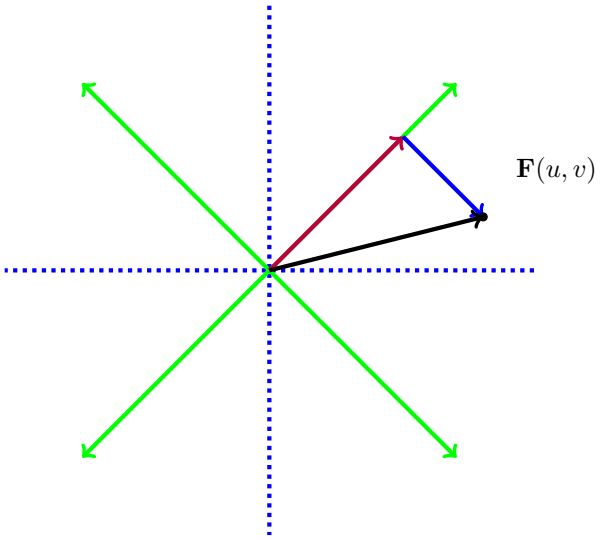

Figure 1. The method used for generating an N-sided prism phase delay maps. The direction vectors (green) point in the direction of the slope of the prism faces and the dotted lines are the prism edges. Point $F(u,v)$ is a pixel in the phase delay map and the purple vector is the projection of F onto the direction vector. The value of each pixel on the spatial filter is the magnitude of the dot product of F and the direction vector.

From the detector image plane images, x and y slope maps are calculated. For the 3-sided prism, the slope maps are defined as,[2]

$$d_x = \frac{3}{2}\frac{(I_3(x,y) - I_2(x,y))}{\sum_{i=1}^{3} I_i(x,y)}, \tag{4}$$

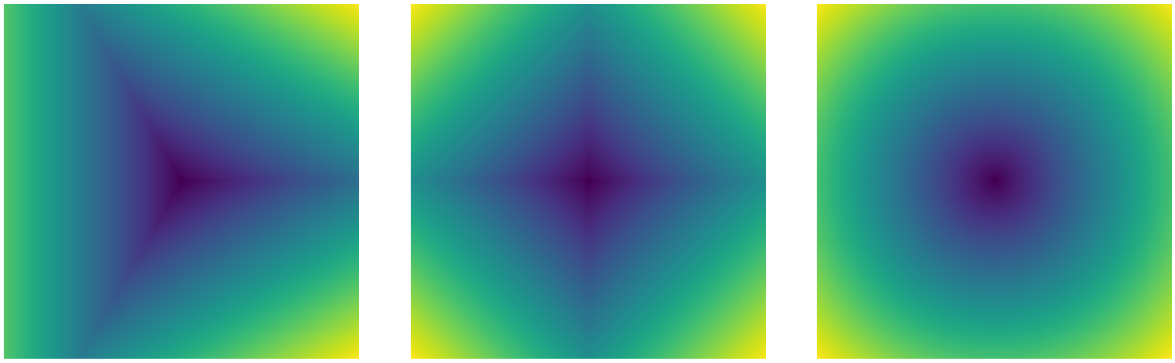

(a) (b) (c)

Figure 2. Simulated prism phase delay maps for (a) a 3-sided prism, (b) 4-sided prism and (c) a cone (∞-sided prism). The phase screen is 1024 by 768 pixels which matches that of the SLM.

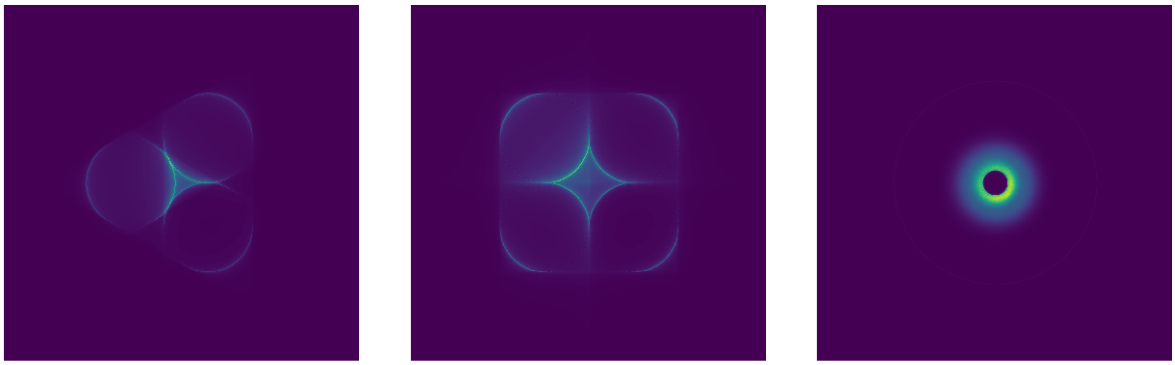

(a) (b) (c)

Figure 3. The simulated WFS detector image plane for (a) a 3-sided prism, (b) 4-sided prism and (c) a cone (∞-sided prism). An aperture diameter of 200 pixels is used, which equates to a 3 mm aperture.

$$d_y = \frac{\sqrt{3}}{2} \frac{(2I_1(x,y) - I_2(x,y) - I_3(x,y))}{\sum_{i=1}^{3} I_i(x,y)}. \tag{5}$$

and for the 4-sided prism the slope maps are defined as,[1]

$$d_x = \frac{I_1(x,y) - I_2(x,y) - I_3(x,y) + I_4(x,y)}{\sum_{i=1}^{4} I_i(x,y)}, \tag{6}$$

$$d_y = \frac{I_1(x,y) + I_2(x,y) - I_3(x,y) - I_4(x,y)}{\sum_{i=1}^{4} I_i(x,y)}. \tag{7}$$

At this time, we have not found an elegant method for extracting wavefront slopes from the cone WFS detector images. In the case of the cone WFS, it is possible to do wavefront estimation directly using the WFS detector image.[7]

3. SIMULATION PROCEDURE

A defocus aberration is used as the incoming wavefront, $\phi(x,y)$, and the resulting detector image plane is computed for the 3-sided prism, 4-sided prism and cone WFSs as shown in Fig. 4. Using the detector image

plane, the resulting x and y slope maps are computed for the 3-sided prism and the 4-sided prism and are shown in Fig. 5.

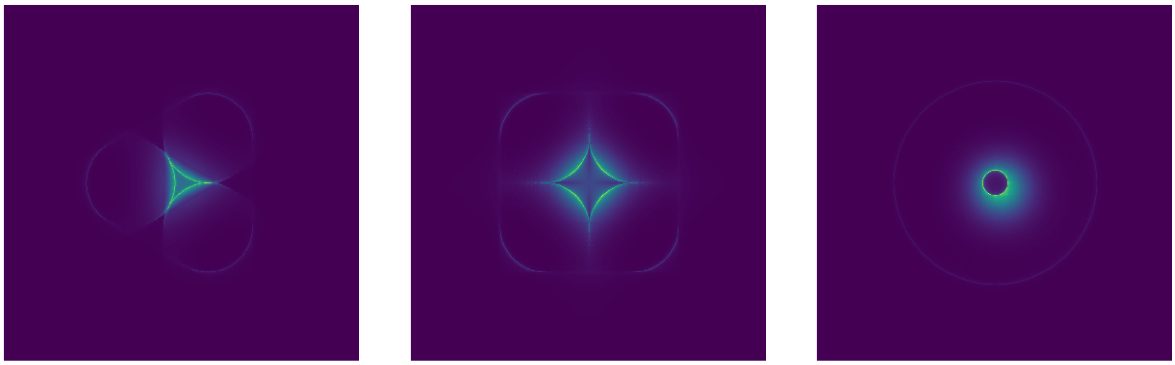

(a) (b) (c)

Figure 4. The simulated WFS detector image plane for (a) a 3-sided prism, (b) 4-sided prism and (c) a cone (∞-sided prism) with a defocus aberration applied.

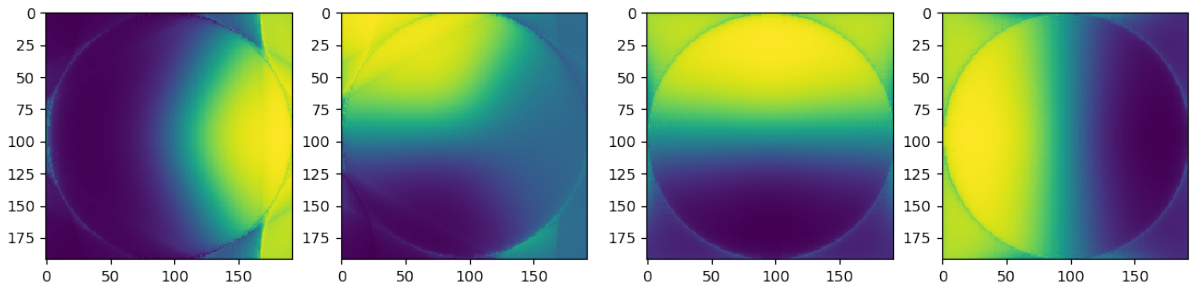

(a) (b)

Figure 5. Using the simulated WFS detector image, the sub-apertures are extracted and the x-slope and y-slope maps are calculated for (a) a 3-sided prism, (b) 4-sided prism, with a defocus aberration applied.

The SLM has a finite number of pixels that can introduce phase delay, and each pixel has a discrete range of phase delay. The phase delay required to produce a prism WFS is larger than the SLM can produce. To overcome this limitation, the phase map needs to be wrapped at the maximum phase the SLM can introduce. To better understand what to expect from an experimental SLM-based digital prism WFS, the resolution of the SLM and the phase wrapping need to be taken into account. Using the prism phase maps from Fig. 2 and applying phase wrapping at the maximum phase shift produced by the SLM (π radians), we produce the phase maps which resemble those which can by realised by a real SLM. The resulting wrapped phase maps are shown in Fig. 6 and the resulting detector image plane is shown in Fig. 7

To measure the linear range of the 3-sided prism WFS, we vary the amplitude of the defocus aberration applied and calculate the resulting x and y slope maps. The magnitude of the resulting slope maps is calculated by finding the projection of the normalised defocus slope maps onto the calculated slope maps. This coefficient should linearly change with the amplitude of the defocus aberration, until the WFS saturates. The resulting dynamic range is shown in Fig. 11a.

4. EXPERIMENTAL PROCEDURE

The SLM used in this paper is a Holoeye LC-R-2500, which has previously been used in the University of Canterbury Electrical and Computer Engineering Optics lab.[8] This SLM has a resolution of 1024 x 768 pixels,

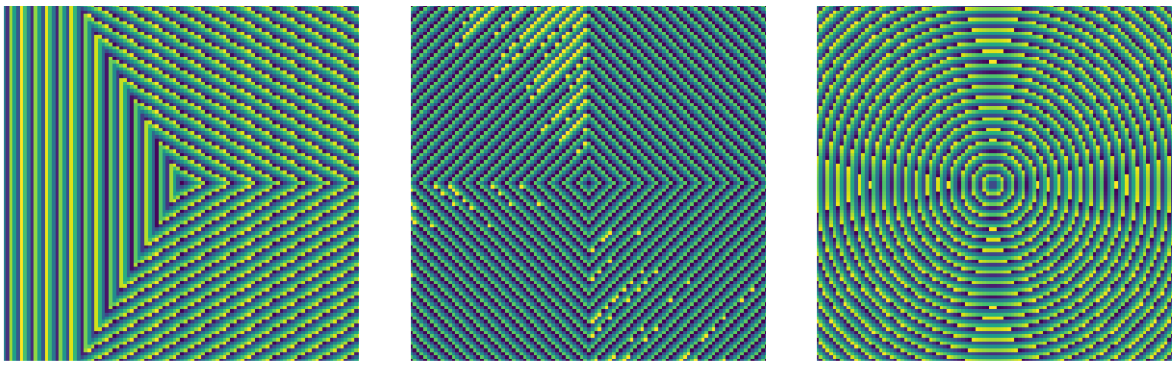

(a) (b) (c)

Figure 6. The SLM used in this paper can produce, at maximum, a phase shift of 1π radians at wavelength of 650 nm. The prism phase delay map requires a maximum phase shift of approximately 300π. To get around this limitation, the prism phase can be wrapped at 1π (the maximum achievable with our SLM). The resulting prism phase screens for (a) a 3-sided prism, (b) a 4-sided prism and (c) a cone (∞-sided prism) are shown. The phase delay maps are zoomed in to a size of 100 by 100 pixels to show the wrapping effect.

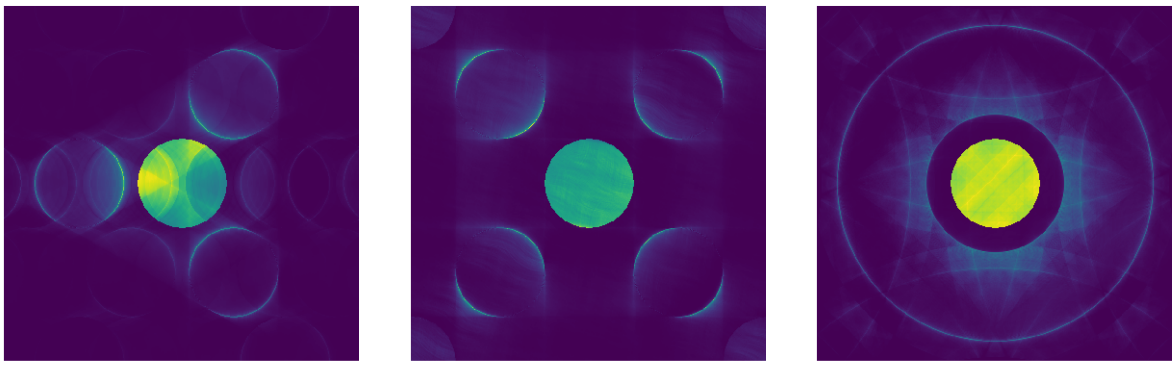

(a) (b) (c)

Figure 7. Using the simulated phase-wrapped prism phase delay maps, the WFS image planes are calculated for, (a) a 3-sided prism, (b) a 4-sided prism and (c) a cone (∞-sided prism). Notice a central sub-aperture and numerous other sub-aperture copies have appeared. This is caused by the diffraction grating effect of wrapping the prism phase delay maps.

with 19 µm square pixels. At 650 nm the SLM can produce a phase delay, at each pixel, of 0-π radians in 256 discrete steps.

A Thorlabs DMP40/M-P01 DM is used to introduce wavefront aberrations. This DM has a pupil diameter of 10 mm, with 24 actuators across the pupil.

A 650 nm semiconductor laser is used as the source, and collimated to a 5 mm diameter beam. The beam is propagated through a polarising filter and onto the DM. From the DM, the beam is propagated through a focusing lens (300 mm focal length). The converging beam passes straight through a beam-splitter and to the SLM, reflecting off the SLM back through the beam-splitter and onto the WFS detector. The optical configuration is shown in Fig. 8.

Using the wrapped phase maps from Fig. 6 and applying them to the SLM, with no aberration applied to the DM, the resulting measured WFS detector images are shown in Fig. 9.

Using the same procedure as in the simulation, a defocus aberration is applied to the incoming wavefront. The DM is used to introduce the aberration. From the WFS detector images, the x and y slope maps can be

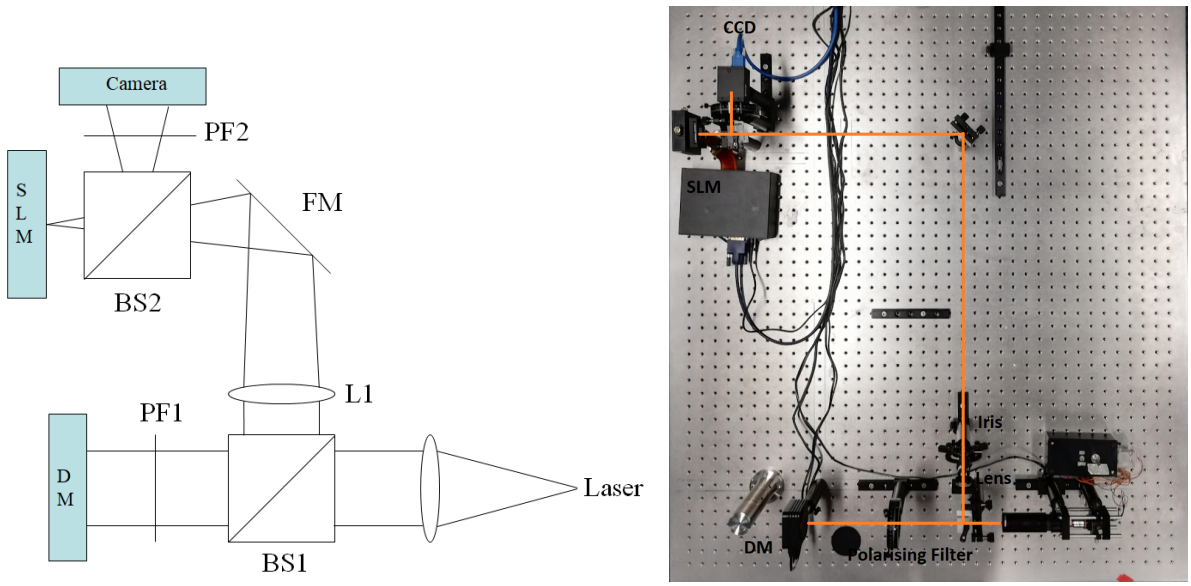

(a) (b)

Figure 8. (a) A schematic of the optical bench configuration and (b) the physical realisation of (a). L1 has a focal length of 400 mm.

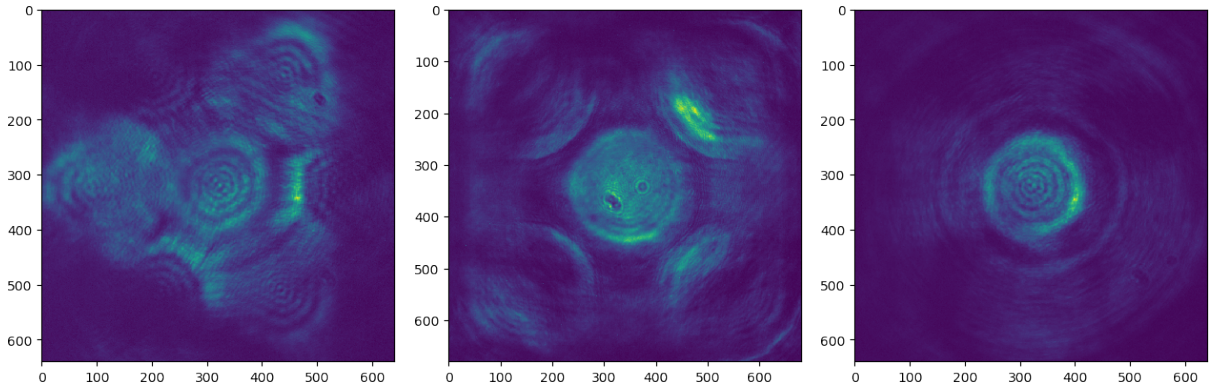

(a) (b) (c)

Figure 9. The measured WFS detector image of a digital prism wavefront sensor for (a) a 3-sided prism, (b) 4-sided prism and (c) a cone (∞-sided prism). An aperture diameter of 3 mm is used.

computed. The resulting x and y slope maps for the 3-sided and 4-sided digital prism WFS are shown in Fig. 10.

The linear range of the digital 3-sided prism WFS is evaluated. The defocus aberration is swept through a range of amplitudes and the x and y slope maps are calculated. From this, the linear range of the WFS can be evaluated. Fig. 11 shows the measured linear range of the digital 3-sided prism WFS compared with the simulated dynamic range for the same sensor.

The measured linearity curve of the 3-sided digital prism WFS is similar to the simulations. This shows that the simulations are accurate and resemble the real system. It should be noted that the phase delay the SLM introduces is wavelength dependent as well as only affecting certain polarisations of light. Due to these limitations, it would be impractical to use this system on-sky. However, it does provide a good toolbox for rapidly evaluating prism-based wavefront sensors.

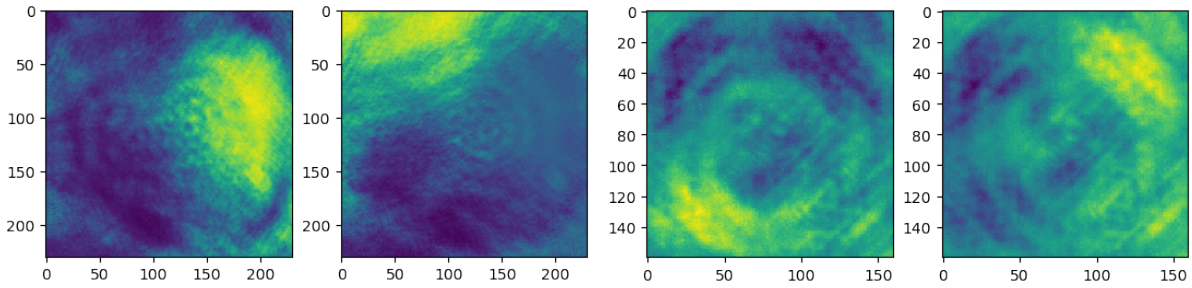

(a) (b)

Figure 10. Using the measured WFS detector images produced by the digital prism wavefront sensor, the sub-apertures are extracted and the x-slope and y-slope are calculated for (a) a 3-sided prism, (b) 4-sided prism with a defocus aberration applied. An aperture diameter of 3 mm is used.

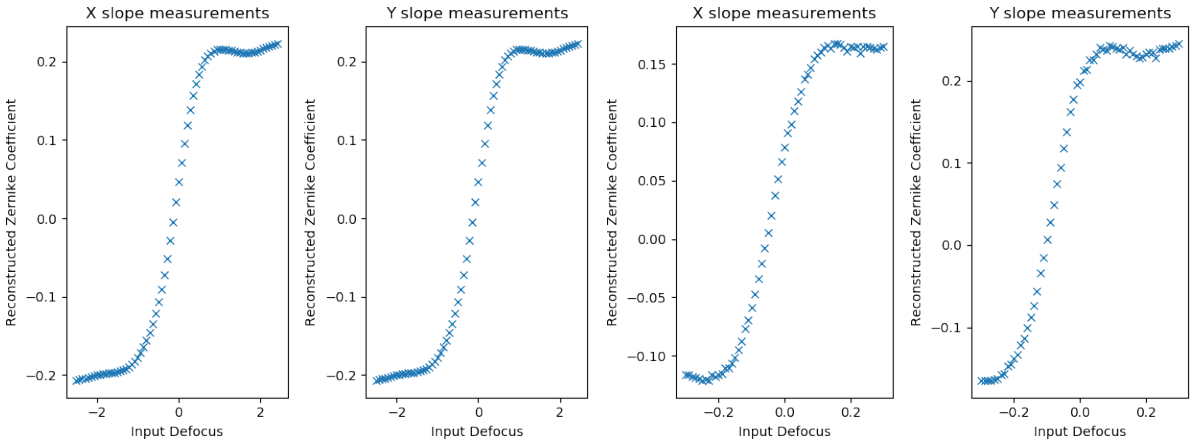

(a) (b)

Figure 11. A defocus is applied to the DM. For the 3-sided digital prism WFS detector images, the x and y slopes are calculated. In simulation, the x and y slopes for the same defocus aberration are calculated. Using a least squares fit, the simulated slopes are fitted to the measured slopes. The amount of defocus is varied and the coefficient of the fit is plotted. (a) The resulting linearity curve from a simulated 3-sided digital prism wavefront sensor. (b) The linearity curve of our physical implementation of a 3-sided digital prism WFS using a SLM

5. CONCLUSION

We created a framework for simulating digital prism-based WFSs as well as creating a physical digital prism-based WFS test bench. In simulation, we have evaluated the dynamic range of the 3-sided digital prism WFS and compared it to actual measurements from the laboratory. For the 3-sided digital prism WFS, the results match closely. The simulation takes into account the limitations of the SLM used in the laboratory, the resulting simulated WFS detector images include the diffraction artefacts caused by wrapping the prism phase delay map and closely resemble the WFS detector images captured in the laboratory.

Our laboratory configuration is in the process of being upgraded. A new Holoeye Pluto-2 SLM will be used. With the new SLM, each pixel can produce more than 2π radians of phase shift, which will allow us to wrap the prism phase delay maps at 2π radians. A Thorlabs Shack-Hartmann WFS (WFS20-7AR) will also be added in parallel with the the digital prism WFS. This will be used as a truth sensor to compare with the results of the digital prism WFS. We also plan to investigate the sensitivity of the different geometry prisms to segment piston modes.[9]

REFERENCES

[1] Ragazzoni, R., "Pupil plane wavefront sensing with an oscillating prism," *Journal of Modern Optics* (1996).

[2] Clare, R. M. and Lane, R. G., "Wavefront sensing from spatial filtering at the focal plane," *Proc. SPIE* (2003).

[3] Fauvarque, O., Neichel, B., Fusco, T., Sauvage, J.-F., and Girault, O., "General formalism for fourier-based wave front sensing: application to the pyramid wave front sensors," *Journal of Astronomical Telescopes, Instruments, and Systems* **3**(1), 019001 (2017).

[4] Clare, R. M., Engler, B., Weddell, S., Shatokhina, I., Obereder, A., and Le Louarn, M., "Numerical evaluation of pyramid type sensors for extreme adaptive optics for the european extremely large telescope," in [*Adaptive Optics for Extremely Large Telescopes 5*], (2017).

[5] Akondi, V., Castillo, S., and Vohnsen, B., "Multi-faceted digital pyramid wavefront sensor," *Optics Communications* (2014).

[6] Engler, B., Weddell, S., and Clare, R., "A digital prism wavefront sensor for ground-based astronomical image correction," in [*2018 International Conference on Image and Vision Computing New Zealand (IVCNZ)*], (Nov 2018).

[7] Engler, B., Weddell, S., Le Louarn, M., and Clare, R., "Effects of the telescope spider on extreme adaptive optics systems with pyramid wavefront sensors ," in [*Adaptive Optics Systems VI*], International Society for Optics and Photonics, SPIE (2018).

[8] Weddell, S. J. and Lambert, A. J., "Optical test-benches for multiple source wavefront propagation and spatiotemporal point-spread function emulation," *Appl. Opt.* (Dec 2014).

[9] Engler, B., Le Louarn, M., Vérinaud, C., Weddell, S., and Clare, R., "Pyramid wavefront sensing in the presence of thick spiders," in [*Adaptive Optics for Extremely Large Telescopes 6*], (2019).